Observation of Conductive Interstitial Ga Line Defects in β-Ga_2O_3

Liyan Wang, Shuai Liu, Ziyuan Liu, Mengjiao Han, Jiehui Tian, Yuchuan Xiao, Qitian Chen, Debo Hu, Lizhi Zhang*, Lixing Kang*, Qing Dai**

L. Wang, J. Tian, Y. Xiao, Q. Chen, D. Hu, Q. Dai
CAS Key Laboratory of Nanophotonic Materials and Devices, CAS Key Laboratory of Standardization and Measurement for Nanotechnology, CAS Center for Excellence in Nanoscience, National Center for Nanoscience and Technology, Beijing 100190, China
E-mail: hudb@nanoctr.cn, daiq@nanoctr.cn

S. Liu, L. Kang
Division of Advanced Materials, Suzhou Institute of Nano-Tech and Nano-Bionics, Chinese Academy of Sciences, Suzhou 215123, China
School of Nano-Tech and Nano-Bionics, University of Science and Technology of China, Hefei 230026, China
E-mail: lxkang2013@sinano.ac.cn

M. Han
Bay Area Center for Electron Microscopy, Songshan Lake Materials Laboratory, Dongguan, Guangdong 523808, China

Z. Liu, L. Zhang
Laboratory of Theoretical and Computational Nanoscience, National Center for Nanoscience and Technology, Beijing 100190, China
E-mail: zhanglz@nanoctr.cn

Keywords: wide-bandgap semiconductors, point defects, Ga vacancies, line defects, near-field infrared characterization

Abstract: Beta-phase gallium sesquioxide (β-Ga_2O_3), possessing an ultrawide bandgap and high breakdown voltage, exhibits strong potential for deep-ultraviolet photodetection and high-power electronics. However, nanometer-scale line defects, prevalent in β-Ga_2O_3 growth, degrade device performance by increasing leakage currents and reducing breakdown voltages, thus termed "killer defects". Critically, the impact of these defects at the atomic scale remains unclear due to limited characterization and a lack of detailed understanding. Here, we report the observation of novel conductive atomic line defects within β-Ga_2O_3 nanoflakes using near-field infrared imaging. Combining atomic-resolution imaging with density functional theory calculations, we identify these defects as interstitial Ga atoms migrating along the *c*-axis. These atomic line defects exhibit a broadband infrared response and quenched cathodoluminescence, indicative of significantly enhanced local conductivity. This elevated conductivity enables subsurface near-field detection of the defects and remote excitation of phonon polaritons in a hexagonal boron nitride (*h*BN) capping layer. These findings underscore the distinct conductivity of atomic-scale line defects, emphasizing the need for their controlled management during material synthesis and device fabrication, while simultaneously suggesting opportunities for their exploitation in nanophotonic applications.

1. Introduction

Owing to its ultrawide bandgap and high critical breakdown field,[1-2] beta phase gallium oxide (β-Ga_2O_3) exhibits an ultraviolet (UV) cut-off wavelength as short as 258 nm,[3] a Baliga's figure of merit thousands of times larger than that of silicon,[4] and a Johnson's figure of merit significantly better than those of silicon carbide (SiC) and gallium nitride (GaN).[5-7] These outstanding attributes together with its relatively low wafer production cost using melt-based and epitaxial crystal growth techniques[8-9] make β-Ga_2O_3 prominent in the fourth generation semiconductors[10-11] and promising in a variety of applications such as deep UV solar-blind photodetection,[12-13] energy-efficient high power switching,[14-15] and radio-frequency power amplification.[16-17]

Since crystallographic defects in β-Ga_2O_3 substrates and epitaxy films would generally degrade the material properties thus deteriorate the device performance and reliability,[18-20] defect-free β-Ga_2O_3 wafers are preferred in the device fabrication. However, despite the fact that melt-grown high-quality native substrates have enabled the homoepitaxy of β-Ga_2O_3,[21-23] which in principle can avoid many of the heteroepitaxy-related threading dislocations that have hampered SiC and GaN,[24-25] point defects are inevitable during growth process, or can be unintentionally introduced through various pathways like doping and radiation damage.[26-28] In intrinsic β-Ga_2O_3 crystals, oxygen vacancies (V_O) and gallium vacancies (V_{Ga}) serve respectively as deep-level donors and acceptors, thereby significantly affecting the electrical and optical properties of the material.[29-32] First-principle calculations have revealed that under oxygen-rich growth conditions, tetrahedral gallium vacancies (V_{GaI}) exhibit the lowest formation energy among cation vacancies.[33] However, V_{GaI} is predicted to be metastable, with a tendency to induce a rearrangement of a neighboring tetrahedral gallium atom into an interstitial site, forming a $2V_{GaI}$-Ga_i complex.[30, 33-36] Under specific circumstances, these point defects may become unstable and diffuse, binding with other defects,[36-37] ultimately evolving into vacancy clusters and extended defects, such as line defects.[37-39] Nanometer-width line-shaped defects, specifically nanogrooves, have been identified as "killer defects" in β-Ga_2O_3 devices, resulting in increased leakage current and decreased breakdown voltage.[19, 40-42] Understanding whether the line defects remain detrimental when reduced to the atomic scale is essential for refining the material growth process and enhancing device performance. Yet, there have been limited reports on atomic line defects induced by point defects, and an in-depth understanding of them remains scarce.

In this study, we discover a V_{GaI}-induced conductive atomic line defect aligned along the *c*-axis within β-Ga_2O_3 nanoflakes and conduct a thorough characterization of this defect at both

atomic and nanometer scales, by integrating techniques such as scattering-type scanning near-field optical microscopy (s-SNOM), high-angle annular dark field scanning transmission electron microscopy (HAADF-STEM), nano-Fourier transform infrared spectroscopy (nano-FTIR), and cathodoluminescence spectroscopy (CL). Our approach kicks off with experimentally mapping the infrared (IR) response of line defects in β-Ga_2O_3 nanoflakes using s-SNOM. This is subsequently complemented by capturing atomic-level images of the defects projected along the *c*-axis via STEM. We then conduct a thorough structural analysis to calculate the formation energy of interstitial defects neighboring the tetrahedral Ga ions, thereby validating the feasibility of the proposed line defect structure. Following this, we explore the broadband spectral responses of the defect region utilizing nano-FTIR and CL. To elucidate the origin of the defect-induced strong IR response, we simulate the near-field IR response of β-Ga_2O_3 nanoflakes with elevated subsurface local conductivity. By comparing the outcomes of our simulations with those from near-field experiments, we can ascertain the high local conductivity at the defect sites. Our discovery advances the atomic-level understanding of pivotal line defects in β-Ga_2O_3, offering crucial insights for the reliable production of ultrawide bandgap semiconductor materials and devices.

2. Results and discussions

β-Ga_2O_3 has a monoclinic structure with the space group C2/*m*.[43] **Figure 1**a shows its unit cell, where $b \perp a$, $b \perp c$, and the angle between *a* and *c* axes is 103.7°. The lattice parameters are given as a=12.2 Å, b=3.04 Å, and c=5.80 Å.[44] Within this unit cell, there are two crystallographically different Ga atoms (Ga_I and Ga_{II}) as shown in **Figure 1**b. Ga_I forms a tetrahedral arrangement with four O atoms, while Ga_{II} resides in an octahedral arrangement, bonded to six O atoms. Correspondingly, the O atoms have three unique sites: O_I and O_{II} bond to three Ga atoms, while O_{III} bonds to four Ga atoms.[30]

Figure 1c illustrates the experimental setup for near-field IR characterization of a β-Ga_2O_3 nanoflake containing line defects. The incident light interacts with the tip-sample system, scattering elastically (see "Methods" for additional details). The β-Ga_2O_3 nanoflakes under test are grown via chemical vapor deposition (CVD) on a silicon substrate with a 285-nm-thick silica top layer. The nanoflakes exhibit a rectangular morphology, featuring a (100) crystal plane as the top surface, with their shorter in-plane side aligning with the *b*-axis (**Figure S1**). During s-SNOM scanning, an AFM image is always recorded simultaneously to reveal the surface morphology of the sample. **Figures 1**d and **S3** display the AFM image and the corresponding average line profile of the β-Ga_2O_3 nanoflake, respectively, which indicate that there are no

apparent structural defects on the sample surface, and the maximum surface height difference is less than 2 Å (**Figure S3**b). However, in the near-field IR image presented in **Figure 1**e, two extended bright stripes along the *c*-axis are observed at an illuminating frequency of 900 cm^{-1}. The line profile of these stripes (inset in **Figure 1**e) exhibits a localized strong IR response. According to the results of far-field IR spectroscopy (**Figure S**2), the absorption frequencies of β-Ga_2O_3 nanoflakes are below 800 cm^{-1}.[45] Therefore, these bright stripes are not caused by phonon resonance; they are more likely to originate from subsurface line defects aligned along the *c*-axis.

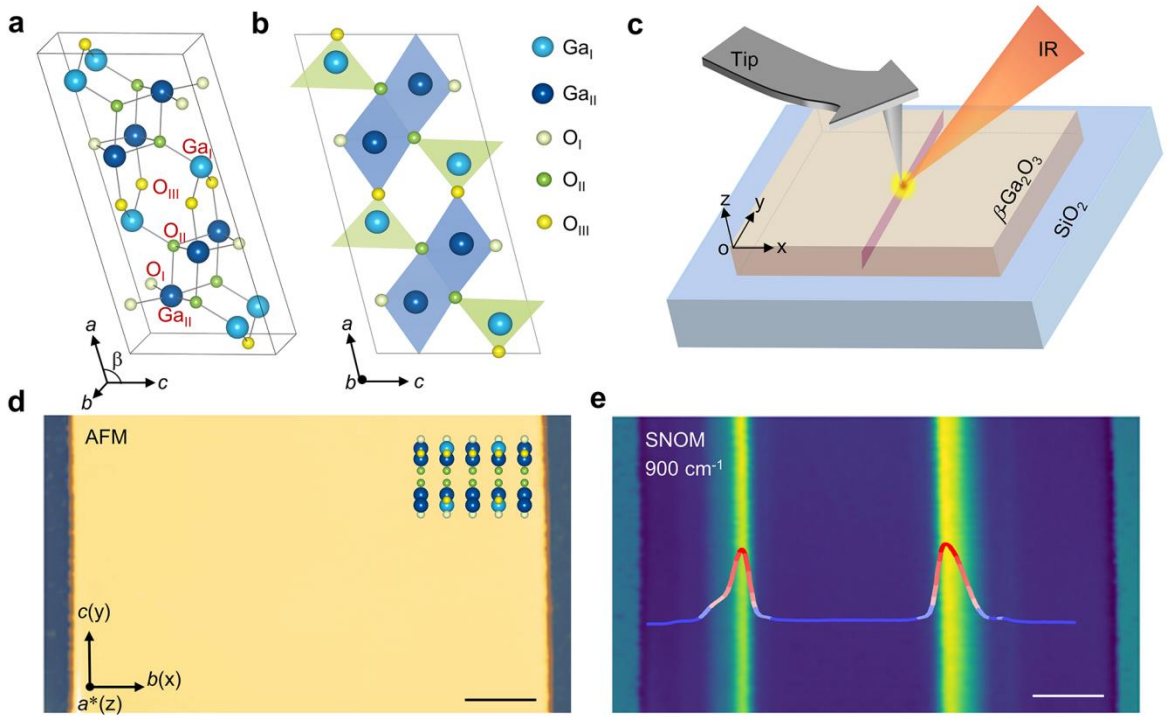

Figure 1. Lattice structure and near-field IR characterization of β-Ga_2O_3. a) Unit cell of β-Ga_2O_3. b) Distinct lattice sites in β-Ga_2O_3: Ga_I is tetrahedrally coordinated and Ga_{II} octahedrally coordinated; O_I and O_{II} are three-fold coordinated, while O_{III} is four-fold coordinated. c) Schematic of the near-field IR experimental setup. d) AFM image of a β-Ga_2O_3 nanoflake. The nanoflake has an atomic-level flat top surface and a thickness of 80 nm. *a**: normal direction of the (100) crystal plane. Inset: atomic structure of the (100) plane. Scale bar: 1 μm. e) s-SNOM image of the β-Ga_2O_3 nanoflake at the illuminating frequency ω=900 cm^{-1}. Two parallel bright stripes along the *c*-axis indicate a strong IR response. The colored line profile depicts the near-field signal intensity along the *b*-axis. Scale bar: 1 μm.

To probe the origin of the observed bright stripes in the near-field IR images, the atomic-scale structure of two (100)-oriented β-Ga_2O_3 nanoflakes, which exhibit similar IR response (insets of **Figure 2**a and **S**4) with that in **Figure 1**, is analyzed using HAADF-STEM. Given the tight atomic arrangement of the (100) plane (**Figure 1**d inset), the HAADF-STEM image is

projected along the *c*-axis. The intensity in the HAADF image, which is proportional to the atomic number, primarily originates from the Ga columns, while O positions exhibit only subtle contrast.[35] Remarkably, extended interstitial defects can be identified along the *a**-axis, as highlighted by the red box in **Figure 2**a. These interstitial defects are positioned between two adjacent Ga_I atomic columns. The intensity profiles of these interstitial columns exhibit an inverse correlation with those of their neighboring Ga_I columns, as illustrated in **Figure 2**b. Specifically, heightened interstitial intensities correspond to diminished intensities in adjacent Ga_I columns. When the intensities are integrated, the combined signal from an interstitial atom column and its two neighboring Ga_I columns is approximately twice as strong as that of a regular Ga_I column. Notably, as the interstitial intensity doubles, the intensities of the two adjacent Ga_I columns nearly vanish, suggesting that the interstitial atoms may arise from the migration of neighboring Ga_I atoms, as illustrated in **Figure 2**c. To further investigate this phenomenon, a 2×4×1 supercell is constructed and an interstitial defect model is designed by displacing two Ga_I atoms (**Figure S**5), respectively. Density functional theory (DFT) calculations reveal the interstitial defect formation energy (E_f) of 0.04 eV per atom, suggesting that the rearrangement of Ga_I atoms is energetically favored.

Since the intensity of HAADF-STEM signals is directly proportional to the total number of Ga atoms [22], the notable increase in intensity observed at interstitial sites in **Figure 2**b indicates the occurrence of multiple Ga_I atomic migrations. This observation implies that Ga_I vacancies may induce a series of atomic rearrangements, leading to the formation of line defects extending along the *c*-axis. **Figure 2**d illustrates two distinct configurations of line defects, characterized by the complete and partial rearrangement of Ga_I atoms. In simulated HAADF-STEM images, full rearrangement appears as a bright atomic column at interstitial sites, with an intensity almost twice that of a normal Ga_I column. Partial rearrangement, however, shows both the original Ga_I columns and interstitial defects (**Figure 2**e, f). Additionally, **Figure 2**a also depicts an extended interstitial defect along the *a**-axis. DFT Calculations reveal that arranging along the *a**-axis has a lower formation energy compared to along the *b*-axis (**Figure S**6). In summary, our findings through HAADF-STEM offer a direct visual representation of Ga interstitial defects within β-Ga_2O_3 and reveal the atomic-scale line defects aligned along the *c*-axis.

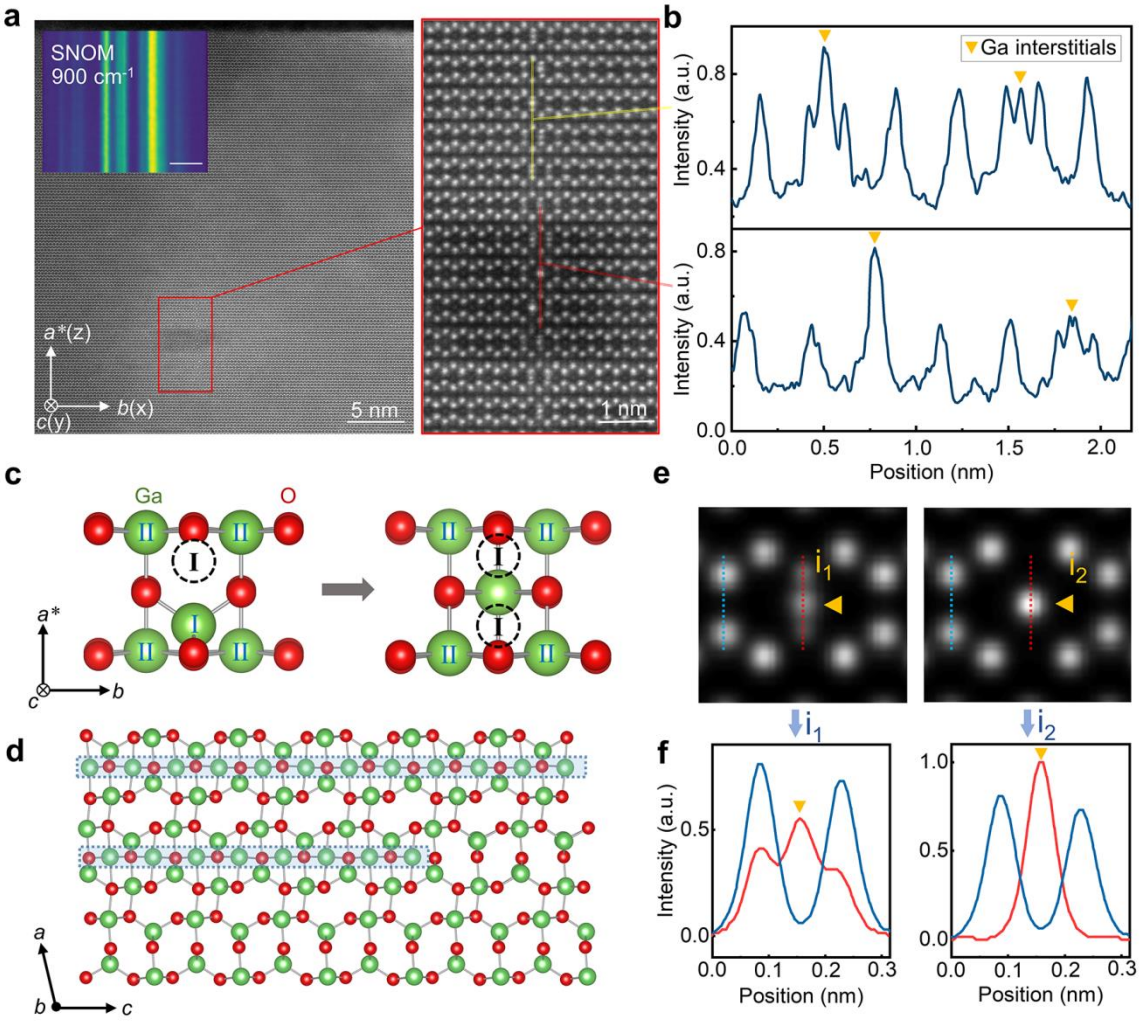

Figure 2. HAADF-STEM imaging and structural analysis of lattice defects in β-Ga_2O_3. a) HAADF-STEM images from a nanoflake with bright stripes in its s-SNOM image. Inset: s-SNOM image at 900 cm^{-1}. Scale bar in s-SNOM image: 1 μm. Red box: interstitial defects region and its enlarged image. b) STEM line profiles. Intensities are evaluated across the red and the yellow lines, respectively. Yellow triangles: Ga interstitials. c) The formation of a Ga interstitial. The Ga_I atom migrates to an interstitial position and leaves two Ga_I vacancies. Black dashed circle: V_{GaI}. d) The atomic structure of the (010) crystal plane, featuring two atomic line defects. First blue frame: all adjacent Ga_I atoms rearrange into interstitial sites. Second blue frame: only partial rearrangement occurs. The supercell used is 2×4×6. e) Simulated HAADF-STEM images with partial rearrangement of Ga_I atoms (i_1) and full rearrangement (i_2) along *c*-axis, respectively. f) Line profiles from a defect-free (blue-dashed) and defective (red-dashed) region in e. Comparing the i_1 and i_2 interstitial sites (depicted as yellow triangles) with adjacent normal Ga_I columns (blue lines), the intensity of interstitial sites significantly increases due to the migration of Ga_I atoms, and is positively correlated with the number of Ga_I atom migrations.

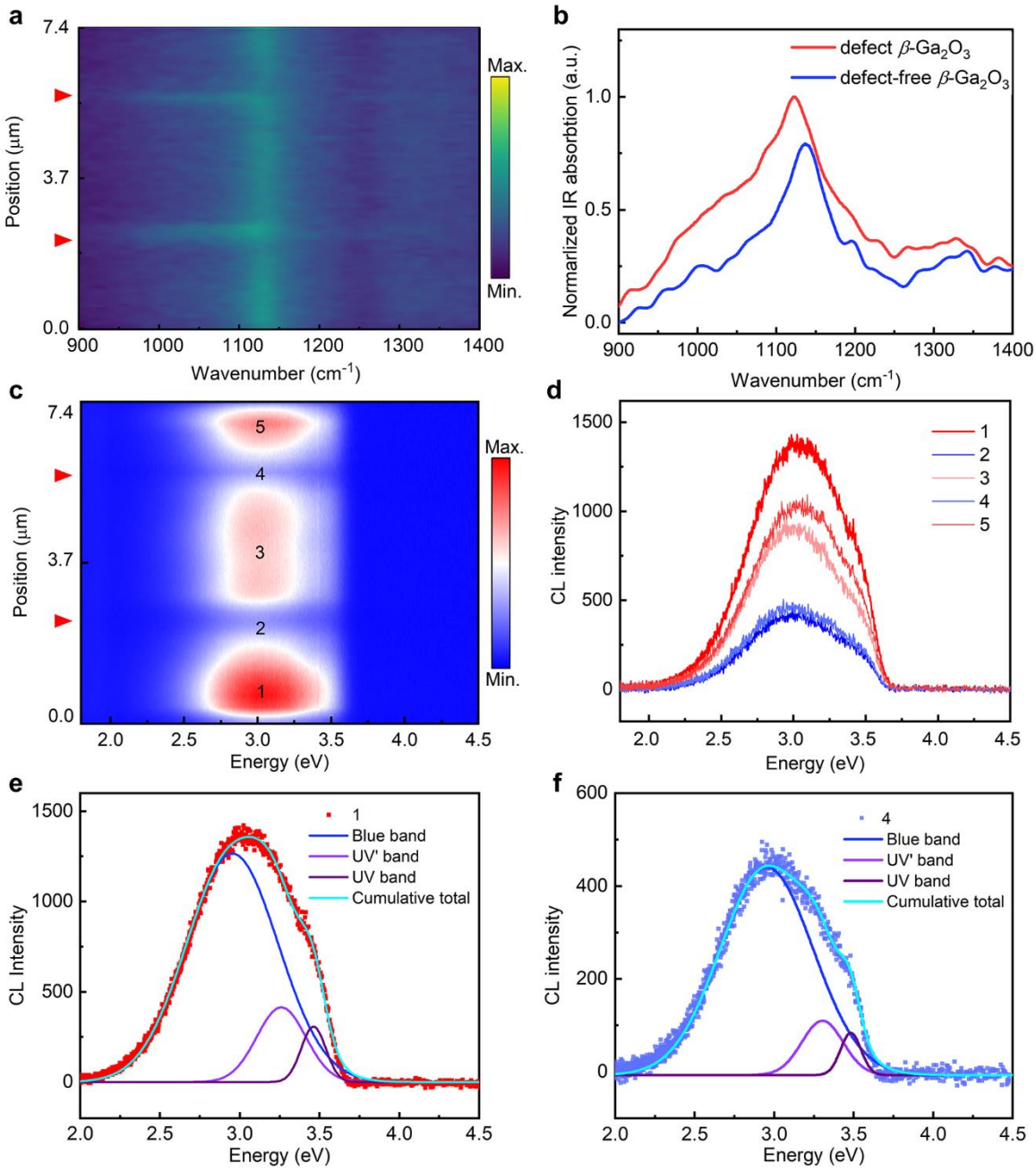

Figure 3. nano-FTIR and SEM-CL spectra of β-Ga_2O_3 nanoflakes with atomic line defects. a) Nano-FTIR line mapping along the *b*-axis, within the frequency range of 900-1500 cm^{-1}. Red triangles: the atomic line defects region. b) nano-FTIR spectra of defect-free and defective regions in a. The defect region displays stronger infrared response. c) SEM-CL line mapping along the *b*-axis, with accelerating voltage of 10 kV, which maps the luminescent properties of defect-free region (1, 3, 5) and defective region (2, 4). d) CL spectra corresponding to the positions 1-5 marked in c. e, f) Multi-peak fitting of the CL spectra at points 1 and 4, respectively. The emission bands can be decomposed into three Gaussian distributions: UV, UV', and blue bands.

To explore the broadband near-field IR response of the same defect region in **Figure 1**e, tunable monochromatic laser and broadband light source are utilized to realize nanoscopic imaging and spectroscopic acquisition, respectively. As depicted in **Figure 3**a, **3**b and **S**7, the nano-FTIR line mapping along the *b*-axis and s-SNOM images both reveal significant enhancement of the optical response within the defect region, spanning from 900 to 1700 cm^{-1}. Notably, the bright band around 1130 cm^{-1} in **Figure 3**a corresponds to the Si-O-Si bond vibration of the silica substrate.[46] By utilizing the signal from the defect-free β-Ga_2O_3 as a reference, we generated a nano-FTIR image (**Figure S8**) that avoids the infrared interference from the silica substrate, thereby highlighting the pronounced broadband IR response specifically in the defective regions. This observation underscores the broadband IR response ($\Delta\omega$ > 800 cm^{-1}) caused by the atomic line defects, which exceeds widths of the Reststrahlen bands for β-Ga_2O_3 (typically spanning several tens of wavenumbers).[45]

Regarding the broadband spectral response of line defects, it can be explained by the frequency-dependent dielectric function of β-Ga_2O_3. Due to intrinsic β-Ga_2O_3 typically exhibits n-type doping. The presence of free carriers can be described by the Drude model, which gives the dielectric function of β-Ga_2O_3 as:

$$\varepsilon_s(\omega) = \varepsilon_\infty\left(1 - \frac{\omega_p^2}{\omega^2 + i\omega\gamma}\right),$$

where ω is the angular frequency, ω_p is the plasma frequency, which depends on the free-carrier concentration n as $\omega_p^2 \sim n$, γ is the damping, which inversely scales with the concentration-dependent carrier mobility $\mu(n)$.[47] The broad-band infrared response enhancement at the line defects in β-Ga_2O_3 is primarily due to the increased plasma frequency ω_p caused by the elevated free-carrier concentration and conductivity. When $\omega < \omega_p$, free electrons in the material resonate under optical excitation, leading to collective oscillations akin to those in metals, enhancing the IR response.[48] Therefore, the enhanced broadband IR response observed at β-Ga_2O_3 line defects can likely be ascribed to an increased ω_p, resulting from a higher free-carrier concentration and conductivity.

To gain a more comprehensive understanding of the optical characteristics of these atomic line defects, we conduct CL imaging and spectroscopy experiments, presenting the respective results in **Figure 3**c and **3**d. The defect regions (labeled 2 and 4) exhibit a significant decrease in luminescence intensity. By fitting the emission peaks of regions 1 and 4 (**Figures 3**e and **3**f, respectively), the emission bands can be decomposed into three Gaussian distributions: UV, UV', and blue bands centered at approximately 3.46 eV, 3.26 eV, and 2.95 eV, respectively.[49] These bands are consistent across both defective and defect-free regions, suggesting a common

luminescent mechanism. When comparing the luminescence intensities of these three bands, the defect region displays a significant reduction of approximately two-thirds. The band structures clearly demonstrate that the presence of Ga interstitials in β-Ga_2O_3 significantly increases the projected density of states (PDOS) around the Fermi level (**Figure S10**), indicating the metallic electronic properties in the line defect regions.[40] Therefore, the presence of Ga-interstitial line defects in a region may lead to enhanced conductivity and suppression of CL luminescence due to decreased radiative recombination.

To confirm that the enhanced IR response of line defects indeed stems from increased local conductivity, electromagnetic simulations for reproducing the near-field imaging contrast are conducted. Based on the subsurface distribution of atomic line defects observed in **Figure 2**a, the region of increased conductivity (50000 Ω^{-1} m^{-1}) is modeled with dimensions of 1 nm in width, 10 nm in thickness, and 30 nm in depth (**Figure S11 and S12**). As shown in **Figures 4**a and **4**b, the simulated surface electric field within this region exhibits a significant enhancement, aligning with the near-field imaging results (**Figure 1**e). Notably, the surface electric field distribution extends over 80 nm (which is 80 times wider than the defect), as illustrated in **Figure 4**a. Thus, despite the line defects exhibiting a 1 nm width along the *b*-axis, which is below the spatial resolution of s-SNOM (~20 nm, determined by the tip curvature), their presence can still be effectively detected through the obvious contrast in near-field imaging. This detection capability arises directly from the enhancement of localized conductivity at the defect sites, generating a pronounced IR response that extends far beyond the physical dimensions of the defects themselves.

To investigate the impact of defect depth on near-field signals and enhance our understanding of s-SNOM's sensitivity in detecting line defects in β-Ga_2O_3 nanoflakes, we conducted further simulations of the surface electric field with varying defect depths. The results shown in **Figure 4**c illustrate that as the defect depth increases from 0 to 55 nm, a notable contrast in the surface electric field persists within the defect region, with an assumed conductivity of 50000 Ω^{-1} m^{-1}. As the depth of defects increase, the surface electric field undergoes an exponential decay (**Figure 4**d), adhering to the attenuation characteristics of near-field signals along the out-of-plane direction. For small variations in conductivity (less than 100 Ω^{-1} m^{-1}), the change in the surface electric field is relatively modest; however, the detection depth can still exceed 25 nm (see inset in **Figure 4**d). On the other hand, conductivity differences exceeding 1000 Ω^{-1} m^{-1} result in significant increase in the surface electric field, thereby enabling a detection depth that surpasses 50 nm. These findings highlight that the near-field technique can effectively detect buried conductivity variations, enabling the detection of

subsurface atomic line defects. This approach provides a universal framework for investigating buried defects in other materials, where subsurface electronic inhomogeneities significantly impact device performance.

To experimentally showcase the enhancement of local conductivity in the defect region, the near-field response of a *h*BN/β-Ga_2O_3 bilayer heterostructure is investigated. Upon covering with *h*BN, the depth of defects in β-Ga_2O_3 increased by 17 nm, resulting in the flattening of the weaker infrared peaks at 900 cm^{-1}, leaving only the originally stronger ones, as illustrated in **Figure S13.** This observation aligns with the simulation results presented in **Figure 4**c, indicating that an increase in defect depth leads to a reduction in the surface electric field and, consequently, a decrease in the near-field contrast. Conversely, within the upper Reststrahlen band of *h*BN (1460 cm^{-1}), the IR response signal, initially absent at 900 cm^{-1}, reappears and undergoes a notable amplification, as shown in **Figure 4**e. The enhanced IR response at the phonon frequency can be attributed to strong interactions between *h*BN phonons, conductive electrons in the defect region, and the scanning probe tip. Furthermore, the line defect boundary in β-Ga_2O_3 can serve as an antenna to excite phonon polaritons in *h*BN, further confirming the significant enhancement of local conductivity at the defect region. By analyzing the response contrast between defects and the induced polaritons in *h*BN, an approximate conductivity for the defect region can be derived, disregarding variations in defect depth. The simulation (details can be found in **Figure S14**) shows a peak conductivity of approximately 30000 Ω^{-1} m^{-1} in the region of strongest IR response, resulting in an electric field distribution that matches the experimental observations (**Figure 4**f).

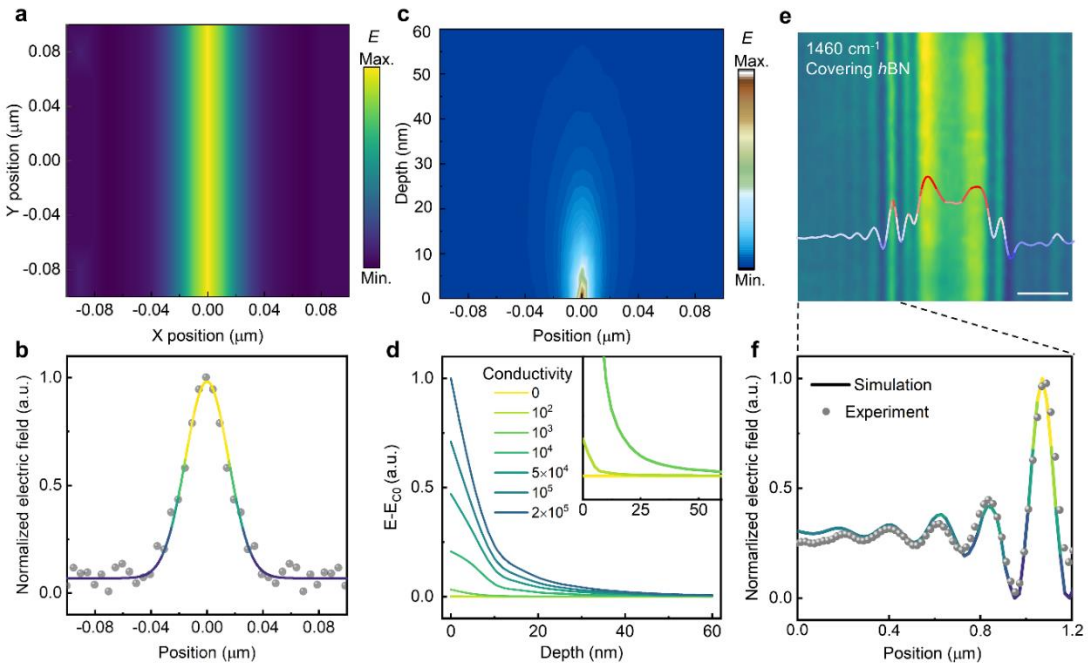

Figure 4. Near-field IR responses of subsurface line defects with increased local conductivity in β-Ga_2O_3. a) Simulated surface electric field distribution in the *xy*-plane, with the defect positioned at the center with a width of 1 nm, a thickness of 10 nm, and a depth of 30 nm. The conductivity in the defect region is set to 50000 Ω^{-1} m^{-1}. b) Line profile of the surface electric field along the *x*-axis in a. The colorful curve is a Gaussian-type peak fitting. c) Surface electric field mapping as the defect depth increases, with a defect conductivity of 50000 Ω^{-1} m^{-1}. d) Comparison of depth dependence of electric field for conductive line defects at various conductivity. Inset: zoom-in view at conductivity range 0-1000 Ω^{-1} m^{-1}. E_{C0}: the electric field when the conductivity is 0. e) Experimental near-field IR response of the *h*BN/β-Ga_2O_3 heterostructure at an illuminating frequency of 1460 cm^{-1}. The thickness of *h*BN layer is 17 nm. The fainter, equally spaced stripes represent the *h*BN phonon polaritons launched by the conductive line defects within β-Ga_2O_3. f) Simulated (solid line) and experimental (scatter plot) near-field profiles of the heterostructure in e. In the simulation, conductive line defects are assumed to be situated at the surface of β-Ga_2O_3, resulting in a primary dependence of the surface electric field on conductivity. The brightest stripe observed in e corresponds to a local conductivity of 30000 Ω^{-1} m^{-1}.

3. Conclusion

Conductive atomic line defects in β-Ga_2O_3 nanoflakes are identified through combined experimental and theoretical investigations. These defects, comprising interstitial sites between two Ga_I atoms and extending along the *c*-axis, exhibit a substantial conductivity enhancement exceeding 10^4 Ω^{-1} m^{-1} within the defect regions, concomitant with an approximately 67% reduction in luminescence efficiency. The formation of these conductive atomic line defects may be linked to thermodynamic fluctuations or variations in carbon dioxide partial pressure during material growth, requiring further mechanistic study. While the enhanced conductivity

could be advantageous for specific applications, it also poses challenges for high-power device reliability due to increased heat generation and dark current. Furthermore, the diminished luminescence efficiency may negatively impact optoelectronic device performance. These findings underscore the critical importance of precise defect control during the growth of β-Ga_2O_3 to optimize device performance. Future research directions include investigating the defect evolution process, developing controlled synthesis methodologies, and exploring local properties such as thermal transport, enabling comprehensive, in situ, and correlative studies of these defects and their impact on device behavior.

4. Experimental Section

Synthesis of β-Ga_2O_3 nanoflakes: β-Ga_2O_3 crystals were synthesized through atmospheric pressure chemical vapor deposition in a heating furnace containing a quartz tube. During the growth process, high-purity metal gallium (99.999%, from Aladdin) served as the precursor. A trace amount of CO_2 was introduced for oxidation purposes, while argon was utilized as the carrier gas. The gallium (10 mg) was positioned in the center of the heating zone, with the substrate situated 5 cm away from the furnace's hottest point. Initially, the furnace was heated under a flow of 200 sccm argon and 100 sccm hydrogen to gradually reach a temperature of 1000 ℃. The introduction of hydrogen ensured that gallium remained unoxidized until the desired temperature was attained. Subsequently, CO_2 (5-30 sccm) was infused into the system. After a growth period of 5 minutes, β-Ga_2O_3 nanoflakes were deposited onto the substrate.

EBSD data collection: EBSD data is collected by an GeminiSEM 300 equipped with NordlysNano EBSD detector. Operating conditions are 70° specimen tilt, 20 kV accelerating voltage, 10 nA beam current, and low vacuum, with a step size of 0.1 μm.

Near-field optical and Nano-FTIR imaging: In the near-field infrared experiments, we employed a commercial SNOM system from Neaspec (https://www.neaspec.com/), which is equipped with both s-SNOM imaging and nano-FTIR functions. The s-SNOM and nano-FTIR setups utilize a continuous wave quantum cascade laser (MIRcat QCL) and an infrared laser continuum generated through difference frequency generation (DFG), respectively. The selection of illumination source is achieved through a flip mirror (FM) and both sources are focused by a parabolic mirror (PM) to illuminate the probe tip. The light backscattered from the tip is then analyzed by a Michelson interferometer, which is operated in either pseudo-heterodyne mode for s-SNOM imaging or as a Fourier transform spectrometer for nano-FTIR

spectroscopy. The interferometer comprises a beam splitter (BS, uncoated ZnSe), a reference mirror (RM) and a detector.[50]

For s-SNOM imaging, the AFM functions in tapping mode. Here, a standard Pt-coated tip (NanoWorld) vibrates vertically with an amplitude of approximately 100 nm at the mechanical resonance frequency of the cantilever (Ω), which is around 260 kHz. The tip is irradiated by the wavelength-tunable QCL. The QCL emits radiation at each single wavelength within the range of 900 to 1700 cm^{-1}, with a power of several milliwatts (mW). The reference mirror (RM) vibrates harmonically with a small spatial amplitude at a frequency ω_m which is much smaller than Ω, to achieve pseudo-heterodyne background suppression. All s-SNOM images presented in this work are obtained by demodulating the total backscattered signal using a lock-in at the third-order harmonic of the tip-tapping frequency, with an integration time of 9.83 ms per pixel. In nano-FTIR spectroscopy, the AFM also operates in tapping mode, with the same vibration frequency and amplitude as those used during s-SNOM imaging. The tip is illuminated by a broadband light source with a power level in the microwatt (mW) range and a frequency range from 800 to 2000 cm^{-1}. The reference mirror scans over a wider spatial range of 600 μm to record the time-domain interferogram (each with a record time of 30 s). By Fourier transformation, the IR spectrum for each pixel can be obtained.

The HAADF-STEM sample preparation and imaging: Focused Ion Beam (FIB) equipped with a Xenon (Xe) ion source was used to prepare STEM samples of cross-sectional β-Ga_2O_3 nanoflakes. Compared with Ga ion, The Xe ion beam can minimize the artifacts and maintain the original structure and morphology of β-Ga_2O_3 samples. The HAADF-STEM imaging of β-Ga_2O_3 nanoflakes cross-section was performed using an aberration-corrected STEM (Spectra 300), operating at 300 kV. The electron probe had a semi-convergence angle of 25 mrad, and the HAADF detector covered an angular range of 36-200 mrad. The HAADF-STEM image simulations were conducted using QSTEM software based on the frozen phonon multi-slice method.[51] The parameters used are shown as follows: the acceleration voltage is set to 300 kV, the spherical aberration Cs is 0 nm, the semi-convergence angle is 25 mrad, the defocus is 0 nm, the source size is 0.8 Å, and the chromatic aberration Cc is 1 mm. The calculated inner and outer collection angles for HAADF-STEM images are 50 and 200 mrad, respectively.

Cathodoluminescence Microscopy: Cathodoluminescence microscopies were conducted using a Tescan Mira SEM equipped with a Gatan monoCL3 and a Goldenscope Rainbow cathodoluminescence module. CL images were captured utilizing a Peltier-cooled GaAs

photomultiplier tube. Spectral acquisition was performed with a CCD detector, employing a 1200 g/mm diffraction grating, achieving a spectral resolution of approximately 0.2 nm under the experimental conditions. All measurements were carried out at room temperature, with an acceleration voltage of 10 kV.

Electromagnetic simulations: The electromagnetic fields were computed using the finite-element method implemented within the COMSOL software package. In near-field optical experiments, a sharp metallic tip was illuminated by an incident laser beam. This tip served as a vertical optical antenna, converting the incident light into a tightly confined near field beneath the tip apex.[52] Consequently, we modeled the tip in our simulations as a vertically oriented (along the *z*-axis) oscillating dipole. During the simulation process, we conducted a point-by-point scan of the dipole along the *x*-axis to emulate the tip scanning process in the experiments. Ultimately, we extracted electric field data from a position located 5 nm above the surface and directly underneath the dipole.

Computational methods: DFT calculations when performing the structural optimization and calculation of defect formation energies were carried out using the Vienna ab initio Simulation Package (VASP)[53-54] with projector-augmented wave (PAW) potentials[55-56] and employing the generalized gradient approximation (GGA) of the Perdew-Burke-Ernzerhof (PBE) function[57]. An energy cutoff of the plane-wave basis was set to 500 eV. Gamma-centered k-point meshes of 3 × 9 × 6, 1 × 3 × 6 and 3 × 3 × 3 are applied to sample the Brillouin zone for the unitcell, and for the 2 × 4 × 1 and 1 × 4 × 2 supercells of β-Ga_2O_3, respectively. And all the structures were fully relaxed until the energy and force converged to 10^{-5} eV and 0.02 eV $Å^{-1}$, respectively. For the band structure calculation as shown in Figure S10, the screened hybrid exchange-correlation functional of Heyd-Scuseria-Ernzerhof (HSE06)[58-59] with functional fraction of Hartree-Fock exchange $\alpha = 0.33$[36] was adopted to obtain a more accurate bandgap. Gamma-centered k-point mesh of 3 × 3 × 3 was also adopted to the density of states calculation.

Supporting Information

Supporting Information is available from the Wiley Online Library or from the author.

Author Contributions

L.W., S.L., and Z.L. contributed equally to this research. Q.D. and D.H. initiated the concept and supervised the experimental procedures. K.L. and S.L. were responsible for the CVD

growth of β-Ga_2O_3 nanoflakes. D.H. and L.W. conducted the near-field infrared and CL measurements. M.H. and L.W. performed the STEM measurements. L.W. carried out the optical simulations. Z.L. and L.Z. executed the DFT calculations. All authors participated in the discussion of the results. L.W. and D.H. drafted the manuscript, with contributions and feedback from all authors.

Acknowledgements

This work was financially supported by grants from the National Natural Science Foundation of China (L2324121, 52072083, 52372055), the National Key R&D Program of China (2021YFA1201500), the Key Research and Development Program of Jiangsu Province (BK20232009), and the Basic Research Development Program of Suzhou (SJC2023004). The authors acknowledge Professor G. J. Zhang of NCNST for assistance with c-AFM measurements and express their gratitude to the Nano-X facility of SINANO for providing technical support.

Conflict of Interest Statement

The authors declare no conflict of interest.

Data Availability Statement

The data that support the findings of this study are available from the corresponding author upon reasonable request.

Received: ((will be filled in by the editorial staff))
Revised: ((will be filled in by the editorial staff))
Published online: ((will be filled in by the editorial staff))

References

[1] H. H. Tippins, *Physical Review* **1965**, *140*, A316.

[2] M. Higashiwaki, K. Sasaki, A. Kuramata, T. Masui, S. Yamakoshi, *Applied Physics Letters* **2012**, *100*, 13504.

[3] S. Oh, M. A. Mastro, M. J. Tadjer, J. Kim, *ECS Journal of Solid State Science and Technology* **2017**, *6*, Q79.

[4] Y. Zhang, J. S. Speck, *Semiconductor Science and Technology* **2020**, *35*, 125018.

[5] S. J. Pearton, J. Yang, P. H. I. Cary, F. Ren, J. Kim, M. J. Tadjer, M. A. Mastro, *Applied Physics Reviews* **2018**, *5*, 11301.

[6] K. D. Chabak, K. D. Leedy, A. J. Green, S. Mou, A. T. Neal, T. Asel, E. R. Heller, N. S. Hendricks, K. Liddy, A. Crespo, N. C. Miller, M. T. Lindquist, N. A. Moser, R. C. Fitch, D. E. Walker, D. L. Dorsey, G. H. Jessen, *Semiconductor Science and Technology* **2020**, *35*, 13002.

[7] M. Higashiwaki, *physica status solidi (RRL) – Rapid Research Letters* **2021**, *15*, 2100357.

[8] Y. Oshima, E. G. Víllora, K. Shimamura, *Journal of Crystal Growth* **2015**, *410*, 53.

[9] S. Rafique, L. Han, M. J. Tadjer, Jr. J. A. Freitas, N. A. Mahadik, H. Zhao, *Applied Physics Letters* **2016**, *108*, 182105.

[10] H. J. G., *IEEE spectrum* **2021**, *58*, 36.

[11] J. S. Speck, E. Farzana, Eds., *Ultrawide Bandgap β-Ga_2O_3 Semiconductor: Theory and Applications*, AIP Publishing LLC, Melville, New York **2023**.

[12] H. Chen, K. Liu, L. Hu, A. A. Al-Ghamdi, X. Fang, *Materials Today* **2015**, *18*, 493.

[13] W. Mu, Z. Jia, Y. Yin, Q. Hu, J. Zhang, Q. Feng, Y. Hao, X. Tao, *CrystEngComm* **2017**, *19*, 5122.

[14] M. Higashiwaki, K. Sasaki, A. Kuramata, T. Masui, S. Yamakoshi, *physica status solidi (a)* **2014**, *211*, 21.

[15] M. Higashiwaki, K. Sasaki, H. Murakami, Y. Kumagai, A. Koukitu, A. Kuramata, T. Masui, S. Yamakoshi, *Semiconductor Science and Technology* **2016**, *31*, 34001.

[16] J. G., C. K., G. A., M. N., M. J., L. K., C. A., T. S., "Gallium oxide technologies and applications", presented at *2017 IEEE Compound Semiconductor Integrated Circuit Symposium (CSICS)*, 2017/1/1, **2017**.

[17] D. C. K., E. W. D., J. G. A., C. A., L. M., L. K., T. S., G. R., A. M. N., J. G., "Sub-Micron Gallium Oxide Radio Frequency Field-Effect Transistors", presented at *2018 IEEE MTT-S International Microwave Workshop Series on Advanced Materials and Processes for*

RF and THz Applications (IMWS-AMP), 2018/1/1, **2018**.

[18] M. Kasu, K. Hanada, T. Moribayashi, A. Hashiguchi, T. Oshima, T. Oishi, K. Koshi, K. Sasaki, A. Kuramata, O. Ueda, *Japanese Journal of Applied Physics* **2016**, *55*, 1202B.

[19] E. Ahmadi, Y. Oshima, *Journal of Applied Physics* **2019**, *126*, 160901.

[20] A. Y. Polyakov, N. B. Smirnov, I. V. Shchemerov, S. V. Chernykh, S. Oh, S. J. Pearton, F. Ren, A. Kochkova, J. Kim, *ECS Journal of Solid State Science and Technology* **2019**, *8*, Q3019.

[21] A. Kuramata, K. Koshi, S. Watanabe, Y. Yamaoka, T. Masui, S. Yamakoshi, *Japanese Journal of Applied Physics* **2016**, *55*, 1202A.

[22] K. Goto, K. Konishi, H. Murakami, Y. Kumagai, B. Monemar, M. Higashiwaki, A. Kuramata, S. Yamakoshi, *Thin Solid Films* **2018**, *666*, 182.

[23] M. Baldini, Z. Galazka, G. Wagner, *Materials Science in Semiconductor Processing* **2018**, *78*, 132.

[24] F. La Via, M. Camarda, A. La Magna, *Applied Physics Reviews* **2014**, *1*, 31301.

[25] I. Akasaki, *Reviews of Modern Physics* **2015**, *87*, 1119.

[26] J. Zhang, J. Shi, D.-C. Qi, L. Chen, K. H. L. Zhang, *APL Materials* **2020**, *8*, 020906.

[27] N. Manikanthababu, H. Sheoran, P. Siddham, R. Singh, *Crystals* **2022**, *12*, 1009.

[28] J. Kim, S. J. Pearton, C. Fares, J. Yang, F. Ren, S. Kim, A. Y. Polyakov, *Journal of Materials Chemistry C* **2019**, *7*, 10.

[29] H. Gao, S. Muralidharan, N. Pronin, M. R. Karim, S. M. White, T. Asel, G. Foster, S. Krishnamoorthy, S. Rajan, L. R. Cao, M. Higashiwaki, H. von Wenckstern, M. Grundmann, H. Zhao, D. C. Look, L. J. Brillson, *Applied Physics Letters* **2018**, *112*, 242102.

[30] M. D. McCluskey, *Journal of Applied Physics* **2020**, *127*, 101101.

[31] M. E. Ingebrigtsen, A. Y. Kuznetsov, B. G. Svensson, G. Alfieri, A. Mihaila, U. Badstübner, A. Perron, L. Vines, J. B. Varley, *APL Materials* **2019**, *7*, 022510.

[32] F. Shi, H. Qiao, *Nano Select* 2021, 3, 348

[33] A. Kyrtsos, M. Matsubara, E. Bellotti, *Physical Review B* **2017**, *95*, 245201.

[34] W. B. Fowler, M. Stavola, A. Venzie, A. Portoff, *Journal of Applied Physics* **2024**, *135*, 170901.

[35] J. M. Johnson, Z. Chen, J. B. Varley, C. M. Jackson, E. Farzana, Z. Zhang, A. R. Arehart, H.-L. Huang, A. Genc, S. A. Ringel, C. G. Van de Walle, D. A. Muller, J. Hwang, *Physical Review X* **2019**, *9*, 041027.

[36] Y. K. Frodason, J. B. Varley, K. M. H. Johansen, L. Vines, C. G. Van de Walle, *Physical Review B* **2023**, *107*, 024109.

[37] K. H. Warnick, Y. Puzyrev, T. Roy, D. M. Fleetwood, R. D. Schrimpf, S. T. Pantelides, *Physical Review B* **2011**, *84*, 214109.

[38] S. Li, Y. Wu, Y. Tu, Y. Wang, T. Jiang, W. Liu, Y. Zhao, *Scientific Reports* **2015**, *5*, 7881.

[39] P. Johannesen, A. Zakrzewski, L. S. Vlasenko, G. D. Watkins, A. Usui, H. Sunakawa, M. Mizuta, *Physical Review B* **2004**, *69*, 045208.

[40] Q. Li, J. Zhao, Y. Li, X. Guan, Z. Jia, N. Lin, X. Zhao, *The Journal of Physical Chemistry C* **2024**, *128*, 11817.

[41] T. Taishi, N. Kobayashi, E. Ohba, K. Hoshikawa, *Japanese Journal of Applied Physics* **2023**, *62*, SF1025.

[42] J. Liu, Q. Li, Z. Han, G. Xu, S. Yang, Z. Zheng, S. Long, in *2024 36th International Symposium on Power Semiconductor Devices and ICs (ISPSD)*, IEEE, Bremen, 2024.

[43] S. Geller, *The Journal of Chemical Physics* **1960**, *33*, 676.

[44] G. Pozina, M. Forsberg, M. A. Kaliteevski, C. Hemmingsson, *Scientific Reports* **2017**, *7*, 42132.

[45] N. C. Passler, X. Ni, G. Hu, J. R. Matson, G. Carini, M. Wolf, M. Schubert, A. Alù, J. D. Caldwell, T. G. Folland, A. Paarmann, *Nature* **2022**, *602*, 595.

[46] R. Hanna, *Journal of the American Ceramic Society* **1965**, *48*, 595.

[47] J. M. Stiegler, A. J. Huber, S. L. Diedenhofen, J. G. Rivas, R. E. Algra, E. P. Bakkers, R. Hillenbrand, *Nano Lett* **2010**, *10*, 1387.

[48] T. Zhang, S. Chen, P. S. Petkov, P. Zhang, H. Qi, N. N. Nguyen, W. Zhang, J. Yoon, P. Li, T. Brumme, A. Alfonsov, Z. Liao, M. Hambsch, S. Xu, L. Mester, V. Kataev, B. Büchner, S. C. B. Mannsfeld, E. Zschech, S. S. P. Parkin, U. Kaiser, T. Heine, R. Dong, R. Hillenbrand, X. Feng, *Nature* **2025**.

[49] M. G. Brik, A. M. Srivastava, A. I. Popov, *Optical Materials* **2022**, *127*, 112276.

[50] I. Amenabar, S. Poly, W. Nuansing, E. H. Hubrich, A. A. Govyadinov, F. Huth, R. Krutokhvostov, L. Zhang, M. Knez, J. Heberle, A. M. Bittner, R. Hillenbrand, *Nature Communications* **2013**, *4*, 2890.

[51] D. A. Blom, T. Vogt, *Advanced Structural and Chemical Imaging* **2018**, *4*, 9.

[52] H. Hu, N. Chen, H. Teng, R. Yu, Y. Qu, J. Sun, M. Xue, D. Hu, B. Wu, C. Li, J. Chen, M. Liu, Z. Sun, Y. Liu, P. Li, S. Fan, F. J. Garcia de Abajo, Q. Dai, *Nature Nanotechnology* **2022**, *17*, 940.

[53] G. Kresse, J. Hafner, *Physical Review B* **1993**, *47*, 558.

[54] G. Kresse, J. Furthmüller, Comput. *Materials Science* **1996**, *6*, 15.

[55] Kresse G, *Physical Review B* **1999,** *59*, 1758.

[56] Blochl P E, *Physical Review B* **1994,** *50*, 17953.

[57] J. P. Perdew, K. Burke, M. Ernzerhof, *Physical Review Letter* **1996**, *77*, 3865.

[58] J. Heyd, G. E. Scuseria, M. Ernzerhof, *The Journal of Chemical Physics* **2003**, *118*, 8207.

[59] J. Heyd, G. E. Scuseria, M. Ernzerhof, *The Journal of Chemical Physics* **2006**, *124*, 219906.

Supporting Information

Observation of Conductive Interstitial Ga Line Defects in β-Ga_2O_3

Liyan Wang, Shuai Liu, Ziyuan Liu, Mengjiao Han, Jiehui Tian, Yuchuan Xiao, Qitian Chen, Debo Hu, Lizhi Zhang*, Lixing Kang*, Qing Dai**

Section I. Confirmation of the orientation and IR spectrum of β-Ga_2O_3 nanoflakes

Before the near-field optical measurements, we preliminarily use X-ray diffraction (XRD) to characterize the crystal structure of β-Ga_2O_3 nanoflakes. As shown in **Figure S1**a, the sharp diffraction peaks observed at 2θ = 30.2° and 45.9° correspond to the (400) and (600) crystal planes of the β-Ga_2O_3 phase,[1,2] indicating a preferential (100) surface orientation of the nanoflakes. The full width at half maximum (FWHM) of the (400) peak is 0.088°, signifying a high crystalline quality of the β-Ga_2O_3 nanoflakes.

We observed the surface morphology of the nanoflakes using electron microscopy. The SEM image of the nanoflake surface and the TEM image of its cross-section are displayed in **Figures S1**b and **S1**c, respectively. The top-view SEM image reveals a uniform and dense surface, while the cross-sectional view TEM image confirms a thickness of ~100 nm without visible cracks or voids.

In **Figure S1**d and **S1**e, we employed electron backscatter diffraction (EBSD) to determine the miller index of the nanoflake top surface. EBSD, integrated with SEM, is a powerful technique for nanoscale crystallographic characterization, offering high spatial resolution (typically <50 nm) to resolve orientation-structure correlations in single-crystalline materials. The methodology hinges on the interaction of a focused electron beam with the near-surface region of a sample, generating backscattered electrons that undergo diffraction to produce Kikuchi patterns. These patterns, composed of intersecting bands corresponding to crystal lattice planes, encode orientation-specific geometric relationships (e.g., interplanar angles, zone axes), which are matched against crystallographic databases to determine local lattice orientations.[3]

For single-crystal β-Ga_2O_3 nanoflakes, EBSD surpasses conventional XRD by eliminating ensemble averaging effects, enabling direct visualization of orientation information at sub-100 nm scales. During the EBSD experiments, the sample was tilted to 70° in the SEM to enhance backscattered electron signals. To mitigate beam-induced damage and ensure surface-sensitive detection, an acceleration voltage of 20 kV and a beam current of 2

nA were employed. A scanning step size (10–100 nm) matching the nanoflake dimensions was applied to collect Kikuchi patterns point-by-point.

To visualize the orientation distribution, inverse pole figure (IPF) maps were generated by projecting crystallographic directions parallel to predefined sample axes onto the crystallographic coordinate system, with data clustering in orientation-specific regions. The inverse pole figure (IPF-Z) in **Figure S1**e reveals that the top surface of the rectangular nanoflakes corresponds to the (100) plane. The nanoflake's long in-plane edge (α=25.2°, long-axis angle relative to sample x-axis) and short in-plane edge (α=115.2°, short-axis angle relative to sample x-axis) orientations maintain preferential alignment along the [001] and [010] crystallographic directions respectively within the crystal reference frame.

After that, we use Fourier transform infrared spectroscopy (FTIR) to obtain the IR absorption peaks of β-Ga_2O_3 nanoflakes, which are located below 800 cm^{-1} (**Figure S2**).

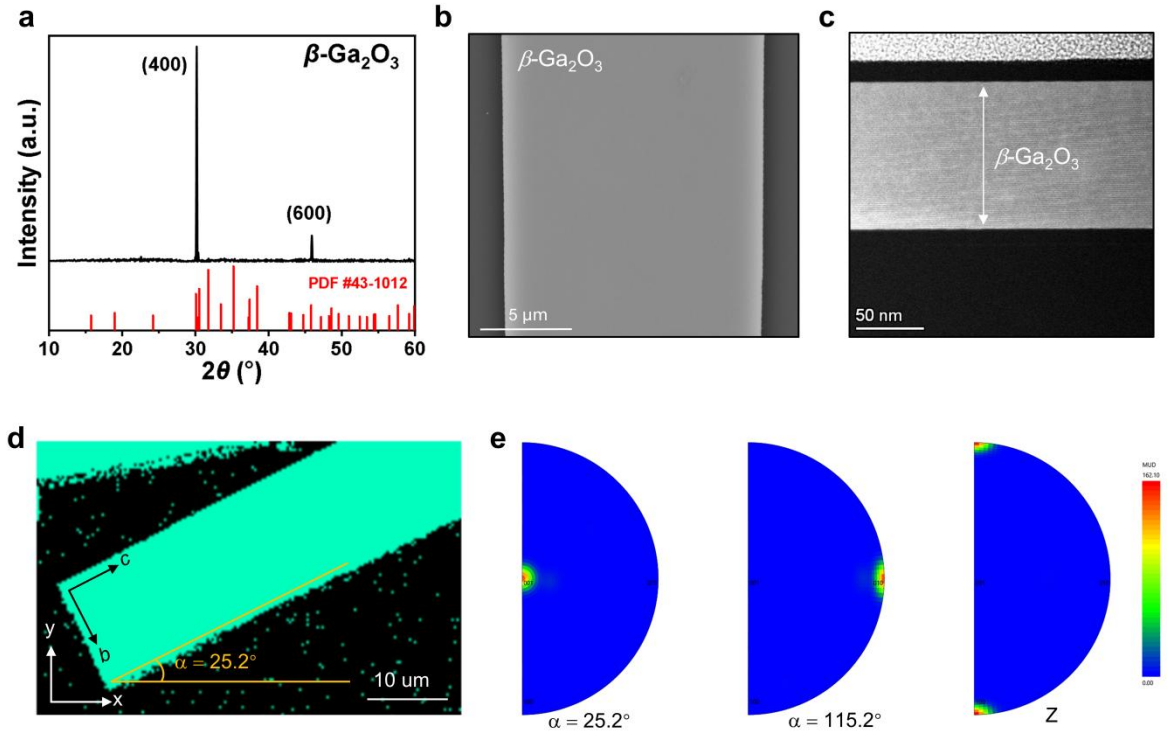

Figure S1. Confirmation of crystal quality and orientation of β-Ga_2O_3 nanoflakes. a) The X-ray diffraction patterns of β-Ga_2O_3 nanoflakes. b) SEM image of the nanoflake surface. c) TEM image of the cross-sectional view of the (001) plane. d) Phase analysis. Green region: β-Ga_2O_3. The angle between the long side of the nanoflake and the x-axis is 25.2°. e) Inverse pole figure (IPF) of the nanoflake in a. IPF is a stereographic projection distribution map that represents the appearance directions corresponding to β -Ga_2O_3 nanoflakes in a crystallographic orientation coordinate system. α=25.2°: the projection direction is along the

longer in-plane side of the nanoflake. α=115.2°: the projection direction is along the shorter in-plane side of the nanoflake (which is perpendicular to the long side, forming an angle of 115.2° with the *x*-axis). Z: the projection direction is along the out-of-plane direction.

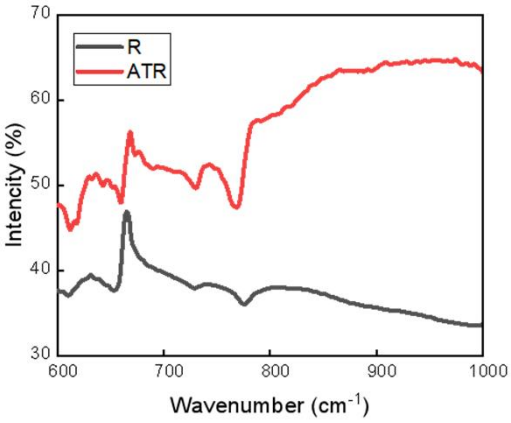

Figure S2. Fourier transform infrared spectroscopy of β-Ga_2O_3 nanoflakes. The infrared absorption peaks are located below 800 cm^{-1}. R: reflection; ATR: attenuated total reflection.

Section II. Analysis of IR enhancement in near-field imaging

As for the microscopic picture of the IR enhancement, we can analyze it from the perspective of the contrast in near-field imaging, which accurately represents the variations in sample permittivity ε_s. Specifically, the point-dipole model can be applied to s-SNOM for data interpretation. In this model, the polarizability α_{ts} of the entire tip-sample system is determined by the equation:

$$\alpha_{ts} = \frac{\alpha_t(1+\beta)}{1-\frac{\alpha_t\beta}{16\pi(a+z)^3}},$$

where a_t refers to the polarizability of the probe, a_t refers to the radius of the apex of the probe tip, z refers to the distance between the tip apex and the sample surface, and β is the static reflection coefficient of the sample surface, which is expressed as:

$$\beta = \frac{\varepsilon_s-\varepsilon_a}{\varepsilon_s+\varepsilon_a},$$

where ε_a is the relative dielectric constant of the surrounding environment of the tip, and ε_s is the relative permittivity of the sample.[4]

The near-field scattering signal E_{ts} has a proportional relationship with α_{ts}. Therefore, it is the ε_s variation caused by the line defects that ultimately leads to an enhancement of the near-field scattering signal.

Section III. Additional experiment data for β-Ga_2O_3 nanoflakes

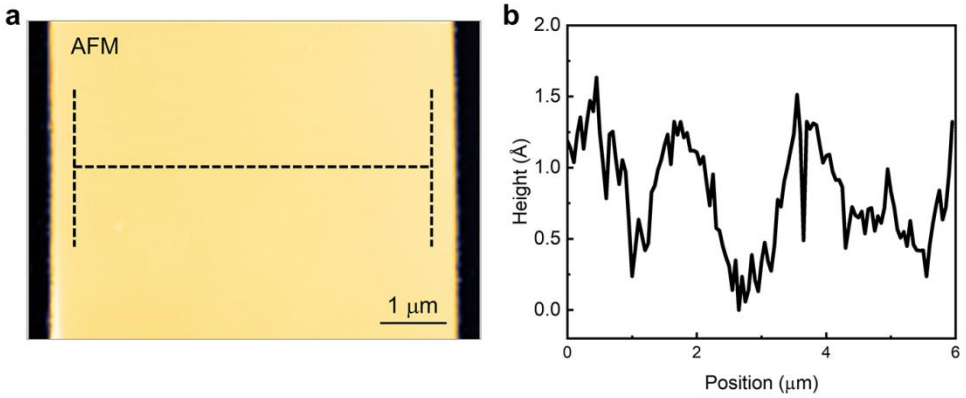

Figure S3. Characterization of surface morphology of the β-Ga_2O_3 nanoflakes. a) AFM image. b) Average line profile of the dashed region in a. The height difference is less than 0.2 nm, revealing an atomically flat surface.

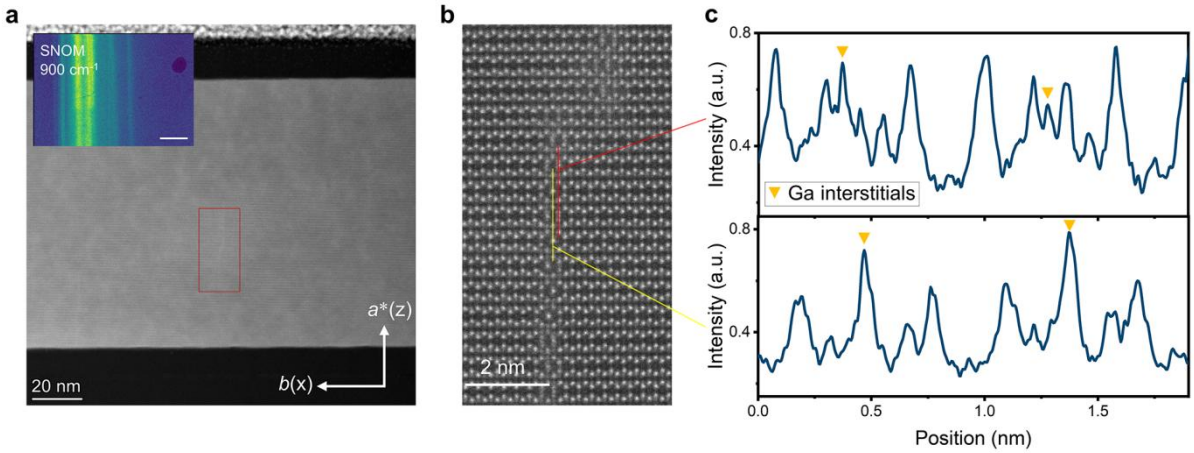

Figure S4. Atomic resolution image and structural analysis of line defects in β-Ga_2O_3 nanoflakes. a) High-angle annular dark field scanning transmission electron microscope (HAADF-STEM) images from a nanoflake with bright stripes in near-field optical image. Red box: extended interstitial defects region. Inset: scattering-type scanning near-field optical microscope (s-SNOM) image at 900 cm^{-1}. Scale bar in s-SNOM image: 2 μm. b) Enlarged image of red box region in a. c) Intensities are evaluated across the red and the yellow lines in b, respectively, showing the significant interstitial defects between the adjacent Ga_I columns.

Section IV DFT calculation of the Ga interstitials

In Figure S5, we construct a 2 × 4 × 1 supercell using theoretical model and design a defect model by moving two Ga_I atoms to the interstitial site. The formation energy E_f of a Ga interstitial is calculated to be 0.04 eV per atom. This E_f is relatively small, indicating that the defect structure is reasonable. Next, we design two extended-defect models and find that the

arrangement of two interstitial defects along *a*-axis is more stable than along *b*-axis, which is consistent with the experimental images in **Figure 2** and **S4**.

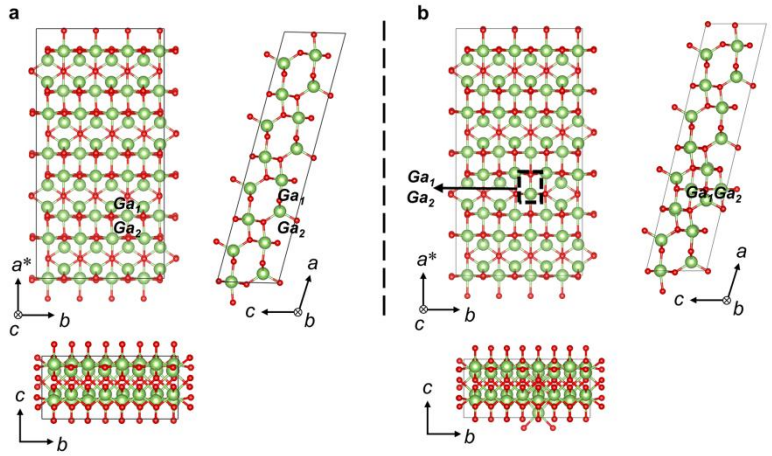

Figure S5. Calculation of the formation energy of a Ga interstitial defect. a) Model without defects. b) Model with a single interstitial defect. Black dashed box: Ga interstitials.

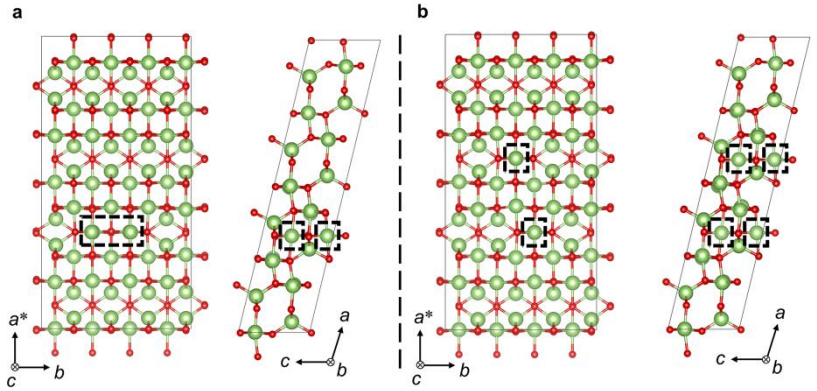

Figure S6. Calculation of the energy of extended Ga interstitials along different directions. a) Model with two Ga interstitials extended along the *b*-axis. E_f = 0.603 eV per atom. b) Model with two Ga interstitials extended along the *a*-axis. E_f = 0.207 eV per atom. Black dashed box: Ga interstitials.

Section V Additional s-SNOM and SEM-CL experiment data for β-Ga_2O_3 nanoflakes.

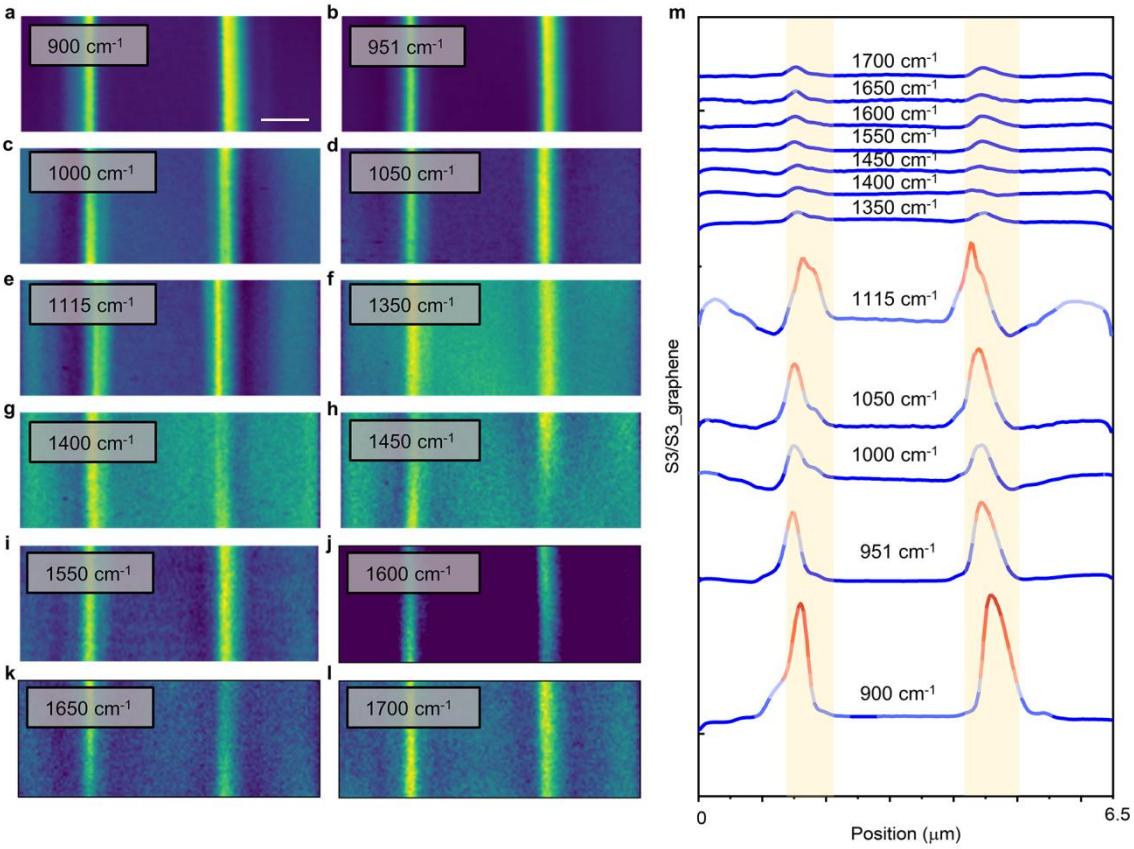

Figure S7. Near-field optical response of line defects in β-Ga_2O_3 nanoflakes with tunable monochromatic laser. a-l) Experimental near-field images from 900 to 1700 cm^{-1} at each single frequency. m) Line profiles corresponding to the near-field images in a-l, the value of signal is normalized to a graphene sample at each frequency. Scale bar: 1 μm.

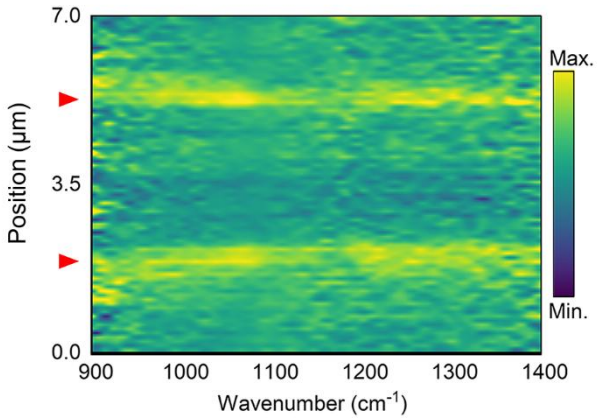

Figure S8. Nano-FTIR line mapping along the *b*-axis, using the signal of the defect-free β-Ga_2O_3 as a reference, within the frequency range of 900-1500 cm^{-1}.

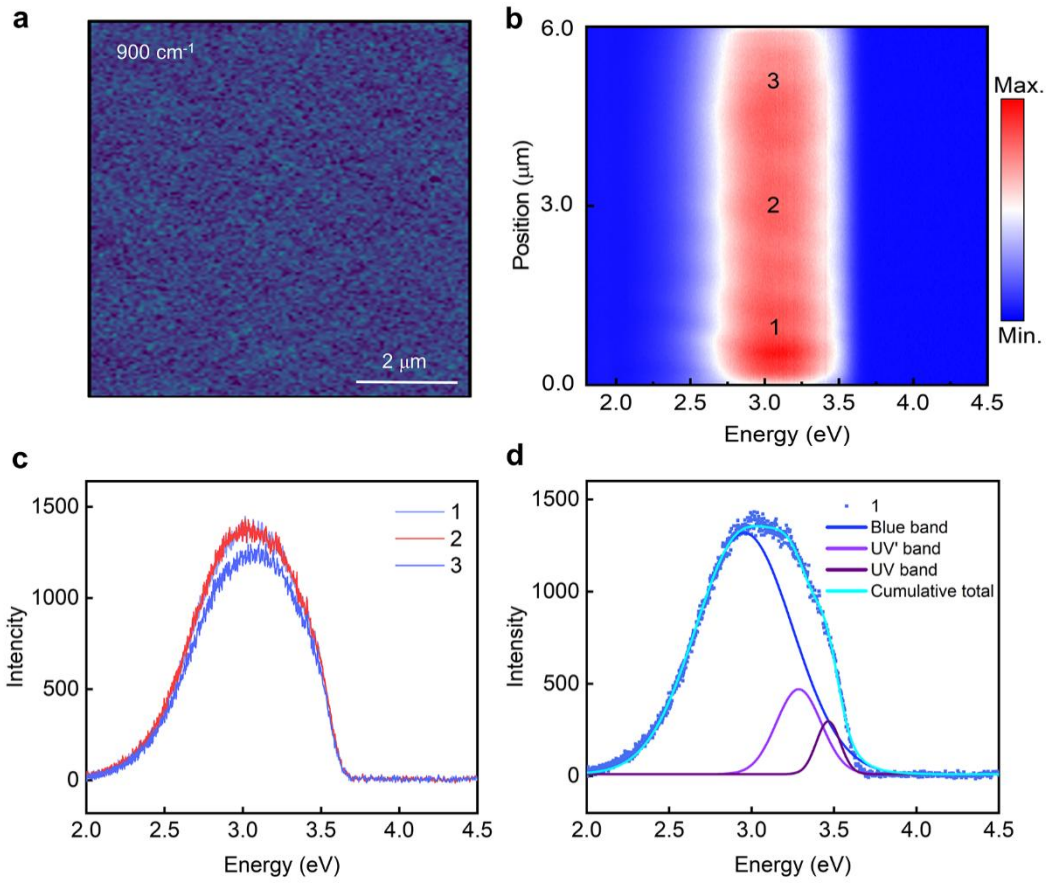

Figure S9. Experimental s-SNOM and SEM-CL imaging of defect-free β-Ga_2O_3 nanoflakes. a) s-SNOM image at the illuminating frequency $\omega = 900\ cm^{-1}$ without bright stripes. b) SEM-CL line profile mapping along the *b*-axis, with an accelerating voltage of 10 kV. c) The spectra corresponding to the positions 1-3 marked in b. d) Performing multi-peak fitting of the CL spectrum at point 1. The emission bands can be decomposed into three Gaussian distributions: UV, UV', and blue bands centered at approximately 3.46 eV, 3.28 eV, and 2.95 eV, respectively.

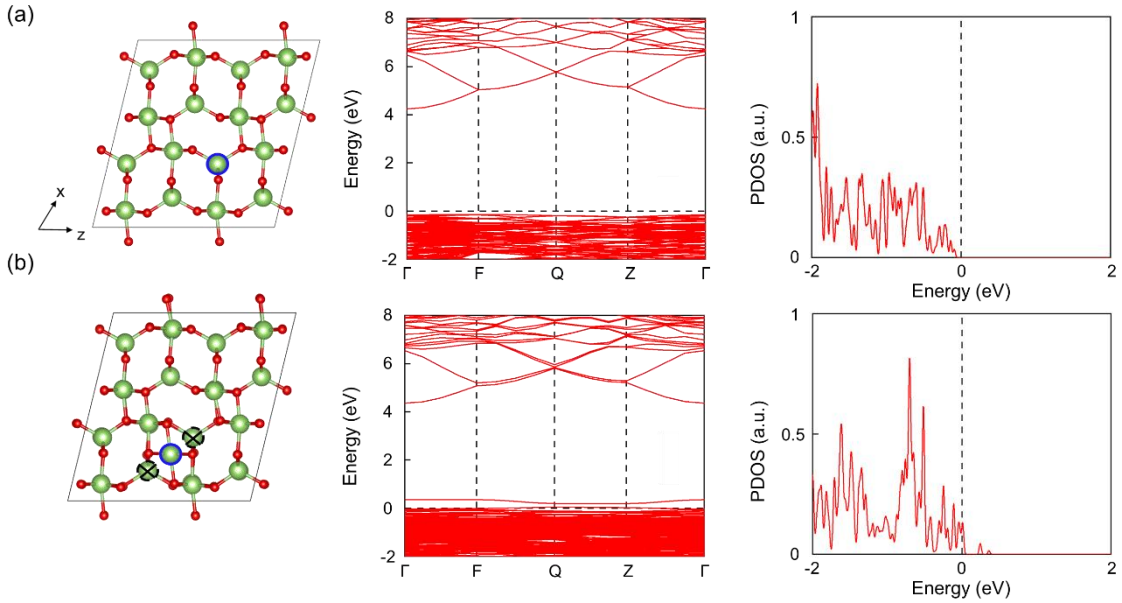

Figure S10 (a) Crystal structures viewed along the [010] direction, band structures calculated by the HSE functional and PDOS of one Ga interstitial atom marked by blue circle of 1 × 4 × 2 β-Ga_2O_3 supercell (a) without and (b) with Ga interstitials.

Section VI Electromagnetic simulation model

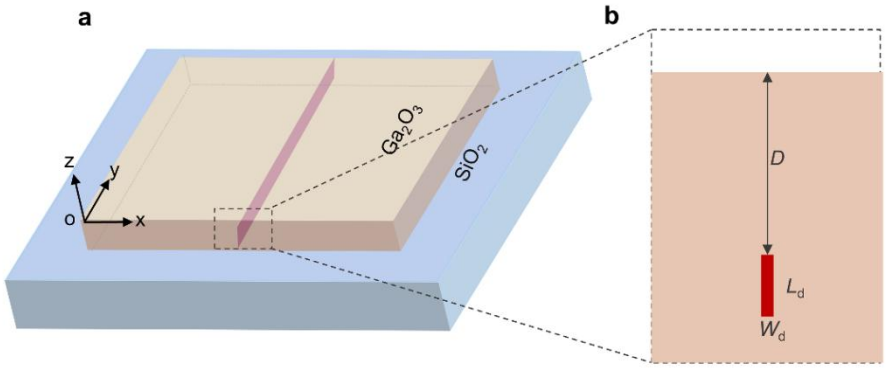

Figure S11. a) Schematic diagram of an electromagnetic simulation model for β-Ga_2O_3 nanoflakes exhibiting increased local conductivity. Substrate: SiO_2. Top layer: an 80 nm thick β-Ga_2O_3 nanoflake. b) Enlarged image of the area with increased local conductivity. Red box: region of increased local conductivity, with a depth D = 30 nm, a length L_d = 10 nm, and a width W_d = 1 nm.

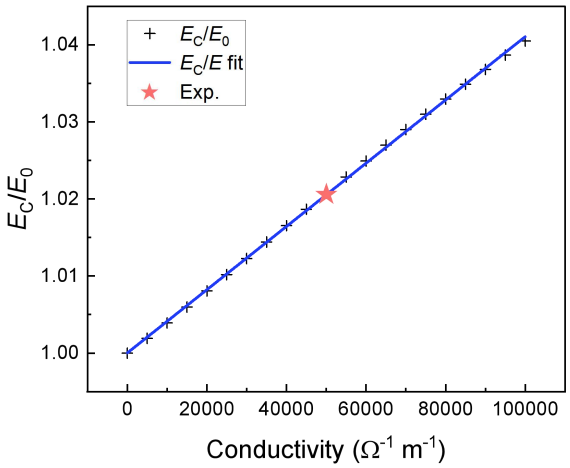

Figure S12 Variation of electric field contrast between defect-free and defective areas as conductivity changes. E_C: electric field with different conductivity. E_0: conductivity is 0 Ω^{-1} m^{-1}. The red star: the ratio of the amplitude of near-field signals between the defective and defect-free areas in Figure 2a.

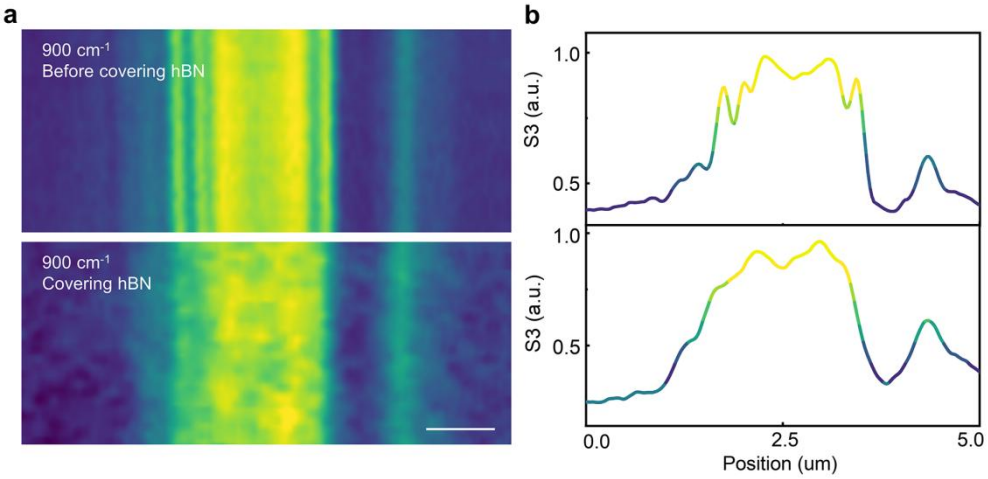

Figure S13 Near-field IR response before and after covering *h*BN. a) Before covering *h*BN. There are obvious boundaries between different bright stripes caused by line defects. b) After covering *h*BN. Narrow bright stripes become blurred and difficult to identify. c) Line profiles of the s-SNOM images in (a) and (b). Frequency: 900 cm^{-1}. Scale bar: 1 μm.

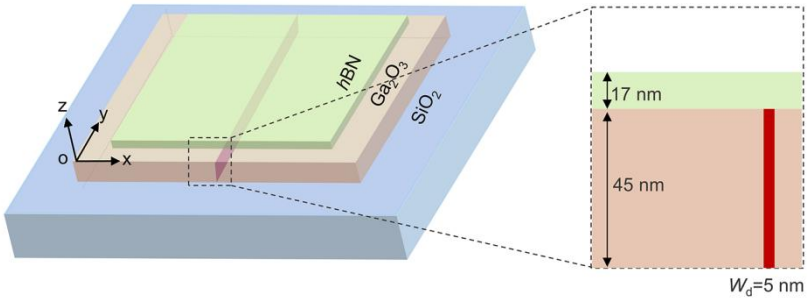

Figure S14 Schematic diagram of an electromagnetic simulation model for the *h*BN/*β*-Ga_2O_3 heterostructure with increased local conductivity in *β*-Ga_2O_3 layer. The *β*-Ga_2O_3 layer is assigned a finite thickness of 45 nm, and the top *h*BN layer is set at 17 nm. The width of defect is 5 nm. Considering that both the defect depth and the conductivity magnitude simultaneously affect the electric field on the *h*BN surface, to simplify the model, we set the height of the defect to be the same as that of the *β*-Ga_2O_3 layer to neglect the influence of the defect depth. By comparing the signal contrast at the defect site with the polaritons of the *h*BN, we can obtain a possible estimation of conductivity value.

References

[1] M. Chen, J. Ma, P. Li, H. Xu, Y. Liu, *Opt. Express* **2019**, *27*, 8717.

[2] X. Li, G. Zeng, Y. Li, Q. Yu, M. Liu, L. Zhu, W. Liu, Y. Yang, D. Zhang, H. Lu, *Nano Res*. **2022**, *15*, 9359.

[3] S. Shekhar, N. K. Sharma, S. Sahu, S. Misra, in Electron Microscopy in Science and Engineering, (Eds: K. Biswas, S. Sivakumar, N. Gurao), *Springer Nature Singapore*, Singapore **2022**.

[4] X. Chen, D. Hu, R. Mescall, G. You, D. N. Basov, Q. Dai, M. Liu, *Advanced Materials* **2019**, *31*, 1804774.